Controlling morphology of polymer particles synthesized from condensed monomer droplets

*Trevor Franklin, Rong Yang**

Robert F. Smith School of Chemical & Biomolecular Engineering, Cornell University, 120 Olin Hall, Ithaca, NY 14853, United States

Abstract:

Non-spherical polymer nanoparticles (PNPs) with tunable morphology are an emerging class of functional materials with enormous potential in drug delivery, sensing, and soft robotics. However, their development is currently limited by the laborious synthesis with limited control over particle morphology. To bridge that gap, we demonstrate the capability of a facile synthesis technique, namely condensed droplet polymerization (CDP) to obtain non-spherical particles with disparate morphologies in a vapor deposition apparatus. The morphological control is enabled by a unique in situ digital microscopy, which reveals the evolution of particle morphology development in real-time, as unreacted monomer was removed from the partially polymerized droplets through evaporation. To guide particle morphology design, the effect of fundamental properties, such as the monomer propagation constant (k_p) and polymer glass transition temperature (T_g), on the resulting particle morphology was investigated using benzyl methacrylate (BzMA, low k_p and low T_g) and acrylic acid (AA, high k_p and high T_g) as examples. Partially polymerized BzMA droplets shrank isotropically during monomer evaporation, giving rise to compact polymer domes, whereas partial polymerization led to a polymerized layer encompassing unreacted AA monomer, which became wrinkled polymer shells or granular particles upon monomer removal. Such insight provides a framework for understanding the fundamental mechanisms of particle morphology formation. The process-property correlations serve to advance the control over polymer morphology in CDP with useful applications ranging from drug delivery to soft robotics.

1. Introduction

Polymer nanoparticles (PNPs) are a versatile class of materials with extensive utility in healthcare (e.g., as drug delivery or theranostic agents)[1–5], chemical sensing,[6,7] carbon dioxide

capture,[8] and antimicrobial technologies.[9] Non-spherical particles, in particular, are desirable as nanomedicines with shapes that elicit a targeted biological response[10–12] and for rheological properties relevant to consumer products, such as the suppression of the "coffee ring" effect that troubles printing technologies.[13–15] Tunability of the morphology of non-spherical particles is critical for their function. For example, aspect ratio of non-spherical particles has been shown to affect the cell type targeted by these particles;[16] particle surface morphology or porosity determines the drug loading and enables tiered release kinetics for programmable pharmacokinetics;[17] curvature of non-spherical particles dictates the metamaterials structure upon particle assembly.[18] While fabrication of non-spherical polymeric particles is commonly achieved only through laborious manipulation of pre-made polymers or through lengthy liquid-based, bottom-up protocols (e.g. seeded emulsion polymerization), these methods afford virtually no control over particle morphology and limited control over particle size or chemical composition.[14,19–22] To address that critical unmet need, here we demonstrate the capability of a facile synthesis technique, namely condensed droplet polymerization (CDP) to obtain non-spherical particles with disparate morphologies. The work reported here also represents an initial step towards building a theoretical framework to understand the reaction-diffusion mechanisms in a polymerizing micro-drop. The insights into how monomer and polymer properties, such as monomer propagation constant (k_p) and polymer glass transition temperature (T_g), dictate the particle morphology set the foundation for understanding the process-property correlations that guide the design of non-spherical polymer particles with controlled morphology.

CDP, a chemical vapor deposition (CVD)-derived technique, has been developed recently to obtain non-spherical PNPs from vapor-phase precursors (e.g., monomer) within minutes. Distinct from prior CVD technologies that afford access to only inorganic nanoparticles,[23,24] or

form particles at a liquid or templated interface,[25,26] CDP achieves non-spherical PNPs without reliance on solvents or structured templates.[27] The steps in CDP feature markedly distinct elements compared to conventional solution-based methods. In the first step, a monomer is vaporized and delivered to a vacuum reactor chamber to condense on a cooled substrate in a dropwise fashion;[28] in the second step, free radicals are generated (by passing a vapor-phase initiator through a heated zone), which rapidly initiate chain-growth polymerization in the monomer drops, forming PNPs in less than one minute. Despite the facile synthesis of non-spherical PNPs using CDP, an understanding of its mechanism is not yet complete, which has limited its potential for enabling control over particle properties that are traditionally challenging to manipulate, such as particle morphology.

In this work, we leverage a unique in situ digital microscopy to observe the evolution of particle morphology development during CDP synthesis in real-time, revealing the importance of the removal of unreacted monomer from the partially polymerized droplets on morphology formation. Building upon this observation, we develop a new framework for understanding CDP by considering the spatial heterogeneity of the degree of reaction within a polymerizing micro-drop, using benzyl methacrylate (BzMA) and acrylic acid (AA) as examples. We demonstrate solid nano/micro-domes for BzMA, due to the solvation of poly(BzMA) (PBzMA) by its monomer, creating an isotropic environment in the polymerizing droplet. Wrinkled shells are obtained using AA as AA undergoes rapid polymerization, which quickly forms a glassy shell around the polymerizing droplet that prevents further initiation by the radicals generated outside the drop. Application of vacuum is used to end the polymerization by removing excess monomers from the polymerizing droplet via evaporation, during which distinct particle morphologies emerge. The effect of spatial heterogeneity of polymerization on particle morphology is illustrated using in-situ

and real-time imaging, which complements ex-situ material characterization. Furthermore, the observations led to a new framework that distinguishes CDP from solution polymerization, i.e., CDP spatially decouples radical generation (which occurs in a separate heating zone) from radical consumption by polymerization, which occurs at temperatures below room temperature in the monomer droplets. The decoupled radical generation-consumption and low-temperature polymerization fundamentally enabled the two pathways described above for a polymerizing drop, each corresponding to a distinct particle morphology. The insights into process-structure-property relationships in CDP that influence particle morphology could guide the future development of non-spherical polymer particles for applications ranging from sensing for cancer treatment[29] to environmental remediation.[30]

2. Experimental Section

2.1 Details of the CDP synthesis

Substrates used in this work consisted of silicon wafers coated with 100-200 nm of smooth poly(1*H*,1*H*,2*H*,2*H*-perfluorodecyl acrylate) (PPFDA) and were prepared in a custom-built initiated chemical vapor deposition (iCVD) reactor according to a previously described protocol.[27] CDP was performed in the same iCVD reactor beginning with the placement of the PPFDA-coated substrate atop a thermoelectric cooling device (TEC, TE Technology) that had been fixed to the reactor stage using a ceramic thermal compound (Céramique 2, Arctic Silver).

The steps of CDP and the process conditions in each step are illustrated in Figure S1. Specifically, the reactor chamber was placed under vacuum and evacuated to approximately 3 mTorr. The reactor stage was cooled by a recirculating chiller (Accel 500 LT, Thermo Scientific) to 10-15 ºC. The TEC was activated to cool below the reactor stage temperature by a DC power

source (1715A, B&K Precision), reaching approximately 4 ºC in the evacuated chamber. A filament array composed of 0.5 mm copper/nickel wire (55% Cu/45% Ni, Goodfellow) positioned above the substrate was heated to above 300 °C. Following the isolation of the chamber by closing a throttle valve (235B, MKS Instruments) at the outlet, monomer vapors were introduced into the reactor through a needle valve. Vapors were generated from liquid monomer stocks by heating benzyl methacrylate (BzMA, Sigma-Aldrich, 96%) to 70-75 ºC or acrylic acid (AA, Sigma-Aldrich, 99%) to room temperature or 40 °C. The flow rate of the monomers varied between 0.1 sccm and 10 sccm during the CDP, which was controlled in real-time while monitoring the size of the monomer droplet using in-situ characterization techniques including an interferometer and a long-focal-length digital microscope (VHX 970F, Keyence). Onset and growth of condensation on the cooled substrate surface occurred once the monomer-dependent saturation pressure was reached. Monomer flow was ceased to halt condensation growth at the desired size. We emphasize that to repeat the work, it is vital to monitor the condensation of monomer drops in real time. The condensation step is highly dynamic, and the monomer drop size distribution depends most strongly on the condensate growth stage (i.e., early stage with simple nucleation versus late stage with drop coalescence), as reported previously in the literature on dropwise condensation.[31–34] The condensation process could enter late-stage growth within seconds. Furthermore, the growth stage is a function of the density of surface nucleation sites, which is substrate dependent. That highly dynamic nature and sensitivity to substrate make it challenging to draw a straightforward connection between the process conditions, like monomer flow rate or chamber pressure, and the resulting polymer dome properties.

Polymerization was instigated by the delivery of unheated *tert*-butyl peroxide (Sigma-Aldrich, 98%) vapor into the chamber through a mass flow controller (1152C, MKS Instruments)

at a rate of 1.8 sccm. The heated filament array thermally decomposed the initiator to form *tert*-butoxyl and methyl radicals to initiate polymerization upon reaching the condensed droplets. CDP was completed by opening the throttle valve to pump away excess initiator vapor and monomer. In situ observations of the polymerization and reactant removal were also enabled by the aforementioned in-situ microscope.

2.2 Chemical characterization of the polymeric domes obtained via CDP

FTIR spectra were collected using a Nicolet iS50 (Thermo Fisher Scientific) spectrometer in transmission mode using a deuterated triglycine sulfate (DTGS) detector. Spectra were collected across the range of 600-4000 cm^{-1} with a 4 cm^{-1} resolution and averaged over 128 scans prior to background correction using a bare silicon wafer and baseline correction using OMNIC software.

Raman spectra and microscope images were collected using a WITec alpha 300 R Raman imaging microscope with a 100x objective. Spectra were recorded using the following settings: 532 nm laser at a power of 2 mW; resolution of 3 cm^{-1} using 300 lines/mm; 10 scans of 10 seconds in duration.

2.3 Morphological characterization of the polymeric domes obtained via CDP

A Zeiss GeminiSEM 500 was used to capture scanning electron microscope (SEM) images with an acceleration voltage of 1 kV. Prior to imaging, samples were coated with approximately 3 nm of gold/palladium.

A ramé-hart Model 500 contact angle goniometer was used to collect monomer contact angles and images of the drop profiles on the PPFDA-coated substrate. Monomer drops of

approximately 5 uL in volume were added to the substrate using a pipette and contact angle measurements were repeated 4 times for each monomer.

3. Results & Discussion

All experiments to observe the polymerization of monomer droplets and formation of polymer particles followed the standard CDP technique (Figure 1A), summarized here. A substrate consisting of a silicon wafer coated with 100-200 nm of PPFDA was placed atop a thermoelectric cooling (TEC) device in an iCVD reactor chamber. The chamber was then evacuated to a pressure of approximately 3 mTorr. Vaporized monomer was metered into the reactor chamber, which subsequently condensed in a dropwise fashion atop the TEC-cooled and PPFDA-coated substrate (Step 1, Figure 1A). Growth and extent of condensation on the cooled substrate was monitored by in situ digital microscopy. To enable the observation of solid polymer particles in Step 3 (described below), BzMA and AA were condensed here until droplets became as large as 25 μm, a scale at which well-defined droplet shapes were discernible by in situ digital microscopy. Condensed droplet growth was subsequently halted by discontinuing monomer vapor flow using a ball valve.

Then, *tert*-butyl peroxide (TBPO) initiator vapor was introduced into the chamber, which formed *tert*-butoxyl (TBO) and methyl radicals upon passing a heated filament array and instigated polymerization upon contact with the droplets (Step 2, Figure 1A). A steady flow of TBPO initiator was maintained for 30 seconds. Notably, this step resembles a bulk polymerization due to the solvent-free nature of the droplet.[35] Radical chain polymerization is a thoroughly-studied reaction mechanism involving radical production, initiation, propagation, termination, inhibition and chain transfer steps (see list of CDP reactions in Table S1).[36]

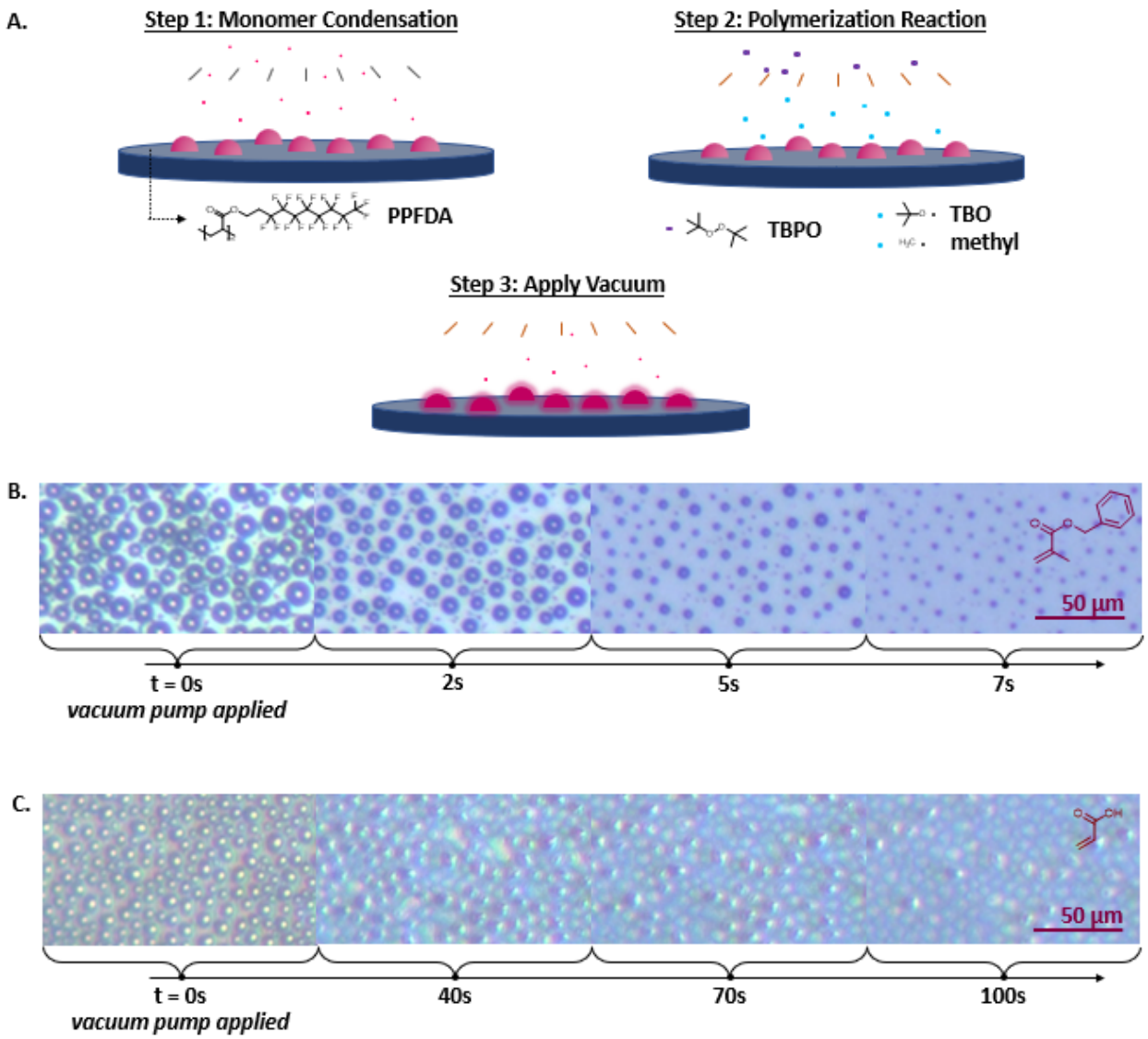

Figure 1. CDP schematic highlighting polymer dome formation. (A) CDP is illustrated via three sequential steps of dropwise condensation of monomer on a cooled substrate, followed by polymerization initiated by vapor-phase radicals, and finally evaporation of unreacted monomer. (B) Microscope images of microdroplet contraction upon monomer evaporation leaving solid polymer domes following application of a vacuum pump during CDP of benzyl methacrylate (BzMA). (C) Microscope images of microdroplet collapsing during monomer evaporation following exposure to a vacuum pump observed in CDP of acrylic acid (AA).

To conclude the polymerization reactions, a vacuum pump was applied to the reactor chamber (after the 30-second exposure to TBPO), which removes excess reactants (e.g., monomer

and initiator) from both the gaseous and liquid phases (Step 3, Figure 1A). Observations of CDP in micrometer-scale droplets indicated an important third step of CDP—monomer evaporation—during which the final particle dome shape was established (Step 3, Figure 1A). Note that this is the first time that this important Step 3 has been identified, representing an important advancement from the previously established two-step protocol. Below, we demonstrate that Step 3 plays a significant role in the resultant particle morphology.

Images of the droplets during monomer evaporation (i.e., Step 3) were recorded in real time, which revealed two distinct modes of evaporation. The partially polymerized BzMA droplets contract isotropically into a compact, solid polymer dome over the course of 7 s due to the evaporation of unreacted monomer from the droplet (Figure 1B). In contrast, as monomer evaporated, the partially polymerized AA droplets flattened onto the underlying substrate without changing their circumference to yield poly(AA) (PAA) shells over the course of 100 s (Figure 1C). Additional contraction of the particles was not observed beyond the timeframes shown in Figure 1B-C, indicating that the bulk of the unreacted monomer evaporated rapidly from the droplets under medium vacuum (3 mTorr). Confocal laser Raman microscopy and Fourier transform infrared (FTIR) of the resulting polymeric microdomes also confirmed that the particles consisted of PBzMA and PAA (Figure S2) and were free of unreacted monomers.

We argue that the degree of solvation of polymer chains by excess liquid monomer in the polymerizing droplet influences the morphology of the resulting solid polymer particles. To explain, we analyze the polymerization mechanism by which monomer converts to polymer in Step 2 and the evaporation of monomer in Step 3 in more detail below. In Step 2, initiator radicals, also referred to as primary radicals, are produced in the vapor phase. The heated filament array creates a heating zone that decomposes TBPO, which is suspended approximately 2 cm above the

droplets, separating the locations of radical generation and of polymerization (Figure 2). This stands in contrast to polymer particle syntheses that occur in liquid environments in which a primary radical is likely formed within the immediate vicinity of monomer molecules and is often a rate-determining step compared to the initiation reaction (e.g., between a primary radical with a monomer).[28,37] Consequently, the production of radicals in CDP is decoupled from the consumption of radicals by the subsequent polymerization reactions.

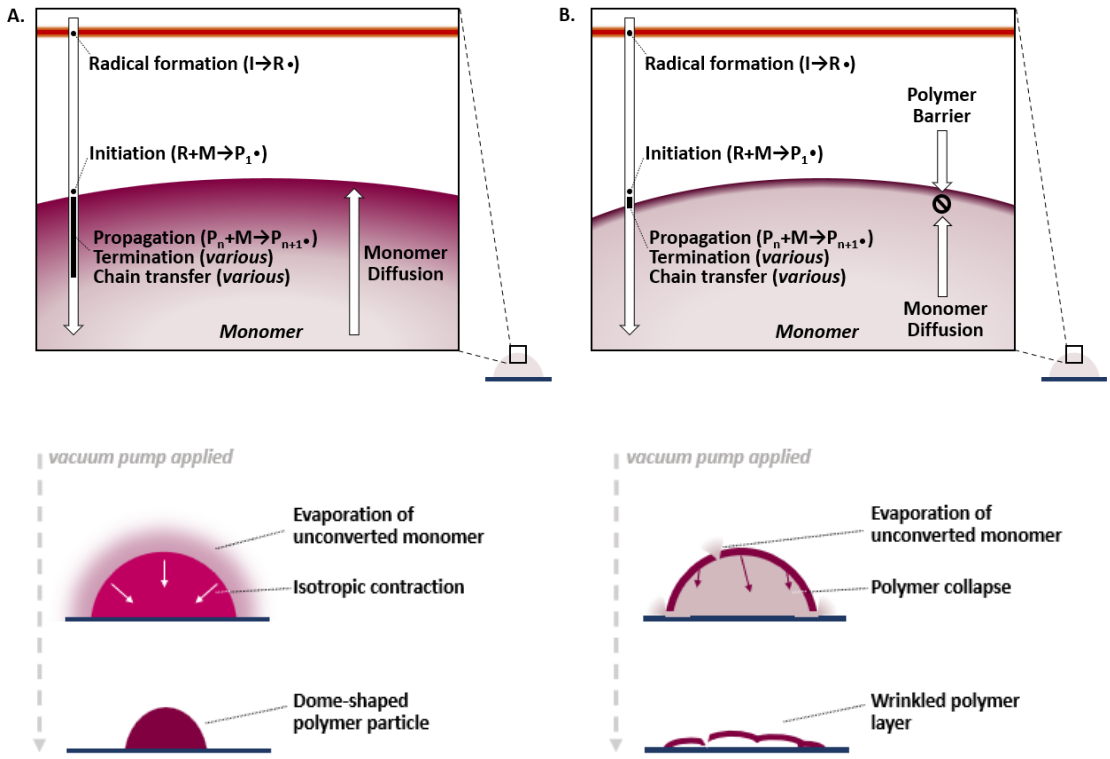

Figure 2. CDP polymerization mechanism in monomer droplets. Two proposed states that influence particle morphology are illustrated in which condensed monomer either (A) readily solvates converted polymer or (B) diffuses slowly into converted polymer. Magnified diagrams of the droplet interface (top) exhibit the layout of the CDP radical chain polymerization mechanism across the vapor and liquid phases. Diagram of the monomer evaporation (bottom) phenomena illustrate the transition to the pure polymer form.

As shown in Figure 2, the primary radicals diffuse in the vapor phase until they reach the surface of a monomer droplet and initiate chain propagation. We postulate that the initiation of propagating chains occurs immediately at the outer surface of the monomer droplets where primary radicals first contact the monomer pool. The diffusion coefficient for an initiator species with a specific volume and molecular weight similar to a monomer can be approximated as equivalent to the diffusion coefficient (*D*) of the monomer, previously calculated to fall in the range of 10^{-8}-10^{-10} cm^2 s^{-1}.[38] Pulsed laser experiments provided evidence of initiation and propagation occurring in less than a microsecond, in which time the mean-squared displacement (MSD), calculated by MSD = 6*D*t,[39] would be < 6 nm at the higher end of the aforementioned *D* range. Thus, propagating chains are believed to predominantly originate at the droplet surface where vapor primary radicals make first contact (assuming chain transfer is negligible). Furthermore, continued chain propagation requires that unreacted monomers are readily available in the vicinity of a propagating chain, i.e., near the droplet surface.

Based on the surface-concentrated initiation events, we attribute the isotropic contraction and the corresponding dome morphology associated with BzMA to the facile diffusion of unreacted monomer to the surface of a polymerizing droplet, where polymer chains forming or formed are well solvated by unreacted monomer. The swelling or plasticizing of polymer chains by unreacted monomer in a partially converted droplet has been demonstrated and well recognized in past studies of emulsion polymerization.[28,40] The effect of that solvation is twofold: (***i***) it enables monomer diffusion towards the droplet surface, fueling continued initiation and propagation; (***ii***) it also drives back diffusion of polymer chains into the droplet, enabling their continued propagation away from the droplet surface. Such exchange is critical to the isotropic transition from a partially converted droplet to a compact polymer particle that occurs upon the removal of

primary radicals and unreacted monomer by applying vacuum (Figure 2A). Specifically, unreacted monomer evaporates upon exposure to the pump and its facile diffusion through a swollen polymer matrix leads to uniform evaporation across the droplet surface. As such, the droplet decreases in size while maintaining the dome shape, which is dictated by the contact angle of remaining liquid BzMA on the non-wetting PPFDA substrate (i.e., 81.3 ± 0.7º for pure BzMA on PPFDA; Figure S2).

To demonstrate that the bulk polymerization of a BzMA droplet occurred under conditions where the polymerizing chains are well solvated by monomers, which are thus less prone to diffusion limitation (Figure 2A), we monitored the conversion of BzMA droplets to polymer domes while varying the reaction time. Specifically, we recorded the evaporation of unreacted monomer from droplets approximately 25 μm in diameter following increasing durations of reaction (Figure 3A). Polymer domes remaining after the evaporation of unreacted monomer were observed to increase in size along with increasing reaction time from 10 s up to 600 s. That increase in size corresponded to an increase in the conversion of monomer in the droplet to polymer and validates the rapid diffusion of monomer to the droplet surface that is required for continued polymerization. The diameters of the bases of four individual particles (approximated to be a circular) were measured before and after the evaporation of excess monomer. The volume of the particles, approximated to be hemispherical, remaining after the removal of excess monomer was calculated, and normalized by the droplet volume (prior to reaction). That percentage droplet volume remaining thus represents the rate of conversion of BzMA monomers to PBzMA (Figure 3B). The polymeric volume of the droplets was only 0.34% after 10 s of reaction and increased to 30.44% after 600 s of reaction.

We further calculated the polymerization reaction rate by dividing the mass of polymerized monomer by the reaction time. To calculate the mass of BzMA converted during polymerization, we made the assumptions that (***i***) domes remaining after monomer evaporation were solid polymer hemispheres consisting only of BzMA units and (***ii***) PBzMA has a density of 1.179 g mL^{-1}. Approximate polymerization rate was calculated to be 1.2×10^{-23}, 0.6×10^{-23}, 1.5×10^{-23}, 2.1×10^{-23}, 2.0×10^{-23} mol s^{-1} for reaction times of 10, 40, 120, 240, and 600 s, respectively. This steady rate across reaction times from 10-600 s supports the hypothesis of swift monomer diffusion to the droplet surface, because any hinderance of monomer diffusion (e.g., at higher conversion) would have slowed down the rate of polymerization over time.

Dome formation and the correlation between reaction duration and extent of droplet polymerization in micrometer-sized particles were consistent at the nanoscale but required ex situ observation. Condensed BzMA droplets of equivalent size that yielded nanoscale particles were polymerized for either 30 s or 2 s prior to scanning electron microscopy (SEM) (Figure 3C). Changes in size at such a scale were not discernible or quantifiable at the resolution of the in situ digital microscope. SEM images showed full, dome-shaped particles from droplets that were initiated for 30 s compared to flatter, smaller particles after only 2 s of reaction.

SEM also revealed evidence of the isotropic particle contraction in the form of particle-free zones around larger polymer domes (Figure 3D). Condensed droplets that coalesced left space for the nucleation and growth of new, smaller droplets which created a characteristic bimodal droplet size distribution.[41] The areas around larger droplets would have been filled by additional droplet nucleation if not for the exposure of that area only at the end of CDP from underneath large partially polymerized droplets upon removal of unreacted monomer. The phenomena of bimodal

particle size distribution at larger scales and the particle-free zones around larger polymeric domes are corroborated by images seen in Figure 3A corresponding to reaction times of 120-600s.

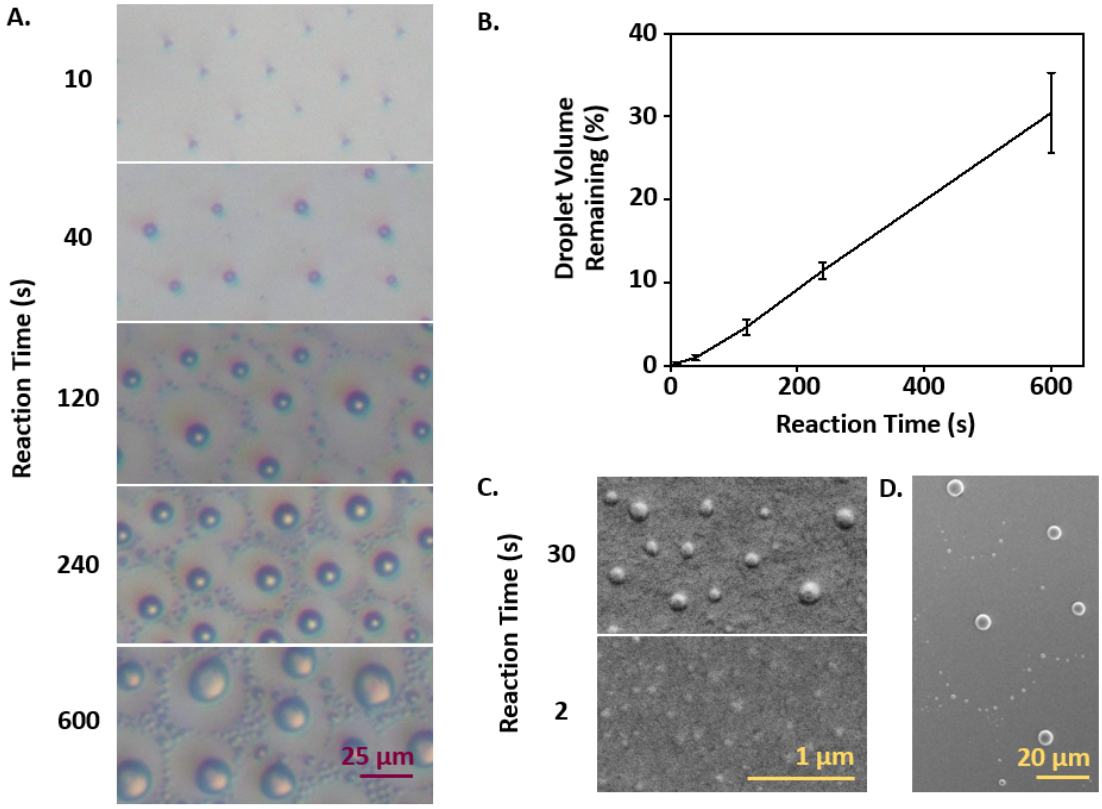

Figure 3. Polymer particle size altered by duration of reaction. (A) In situ digital microscope images of PBzMA particles after the removal of unreacted BzMA monomer by vacuum pump following increasing polymerization reaction times. (B) Plot of droplet volume remaining following removal of unreacted BzMA (droplets approximated as hemispheres with circular bases; line traces mean; bar = SD; n = 4). (C) Scanning electron microscope (SEM) images of PBzMA nanoparticles following polymerization for 30 s (top) and 2 s (bottom). (D) SEM image of PBzMA particles illustrating the particle-free zone surrounding larger droplets resulting from the isotropic contraction of partially polymerized droplets.

In contrast to the isotropic contraction of a partially polymerized BzMA drop, we captured significant changes in the morphology of a partially polymerized AA drop during monomer evaporation (Figure 1C). We attributed that anisotropic morphological change to an alternative

mode of droplet polymerization, which occurs rapidly in a localized fashion near the droplet surface (Figure 2B). This rapid polymerization leads to a high conversion rate, forming a barrier layer that slows the diffusion of monomer towards the drop surface in Step 2 and the monomer evaporation through the drop surface in Step 3. The slowed diffusion at high conversion rates has been observed in emulsion polymerization, during which the effective propagation rates decrease by up to two orders of magnitude, halting the polymerization, as the polymer enters a rigid, glassy state at high conversion.[28,42] Other reports have quantified the monomer diffusivity to be over 6 orders of magnitude lower in glassy polymers than a rubbery polymer.[43]

The high conversion near the droplet surface was likely enabled by the high propagation rate constant, k_p, of AA. Pulsed laser experiments have measured a k_p of 31,200 L mol^{-1} s^{-1} for AA (determined at 20 ºC), over an order of magnitude higher than that of BzMA (1,224 L mol^{-1} s^{-1} as determined at 50 ºC).[44,45] Monomers with high k_p achieves high molecular weight more quickly given comparable rates of initiation and termination,[46] and the glass transition temperature (T_g) is known to be positively correlated to molecular weight, as described by the Flory-Fox equation.[47] Indeed, the T_g of PAA is commonly measured to exceed 100 °C,[48,49] significantly higher than the substrate temperature in CDP (which is cooled to below 10ºC), whereas T_g of PBzMA has been determined to be close to 50 ºC.[50,51] As such, we believe that the rapid polymerization of AA quickly leads to areas of high conversion that exhibit glass-like barrier behavior to subsequent monomer diffusion and evaporation, and that such localized polymerization occurs across the droplet surface. Following the evaporation of unreacted monomer in Step 3, the polymer remains that originated from the droplet surface, featuring parts marred by destructive evaporation events. FTIR confirmed that the wrinkled PAA layers were free of unreacted monomer (Figure S2B). That is why the partially polymerized AA droplets were not compacted to a condensed dome shape like

the case for PBzMA, even though the monomers exhibited similar contact angles on PPFDA substrate (Figure S3).

To further illustrate the morphological ramifications of the rapid and localized polymerization in AA droplets, we mapped partially polymerized micrometer-scale droplets (that were polymerized for 55 s) using atomic force microscopy (AFM). AFM showed that such droplets display a collapsed shell morphology (Figure 4A). Smaller polymer tendrils extending from the PAA canopy and the rough outer edges signified that the primary point of departure of unreacted monomer was at the outer edge of the droplet base (Figure 4A).

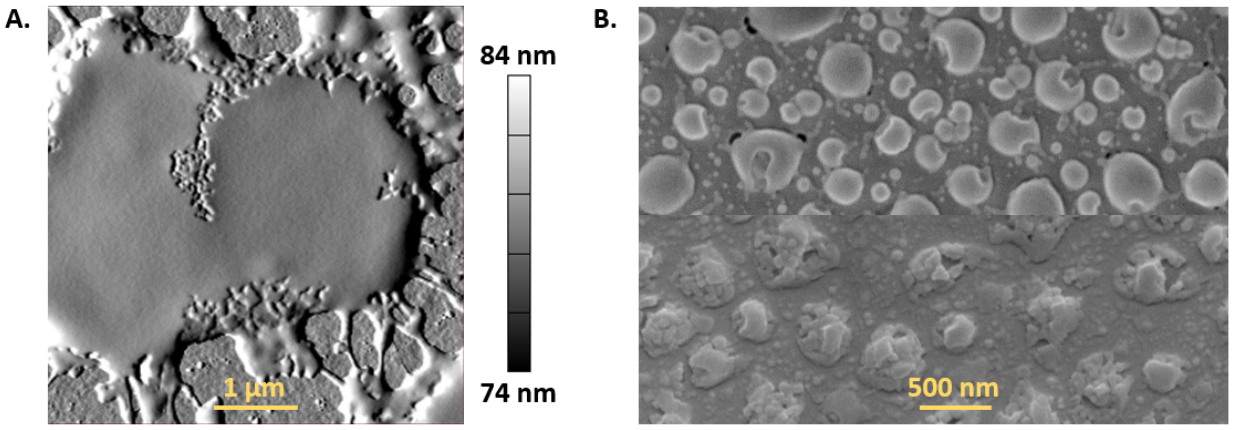

Figure 4. Morphology of PAA after CDP of droplets at the micrometer and nanometer scales. (A) AFM amplitude image of PAA micro-domes obtained via CDP. (B) PAA resulting from CDP of nanoscale droplets displaying punctured shell (top) and granular (bottom) morphologies.

We also captured the morphological structures resulting from CDP of nanoscale AA droplets for comparison with the micrometer scale. SEM images of nanoscale particles (obtained by polymerizing AA droplets for 60 s) also displayed a continuous outer shell (Figure 4B, top), with discernible, individual puncture points that were evident as holes extending up from the

bottom edge of the particle. We believe these puncture points indicate where unreacted monomers escaped the partially polymerized droplets upon application of vacuum. Upon reducing the polymerization time to 40 s (Figure 4B bottom), the continuous outer shell was replaced by a layer of granular particles, which indicates the localized presence of polymers. Compared to the continuous shell formed at 60 s, the granular particles obtained at 40 s represent an earlier-stage growth of the polymer chains, pointing to the localized polymerization prior to the formation of a continuous shell. The localized polymerization could be a result of the rapid rate of polymerization of AA, which drastically increases the viscosity of the polymerizing cluster, preventing the as-formed polymer chains from diffusing away and slowing the diffusion of fresh reactants (monomer and radical) into the cluster to expand its size and delocalize the growth.

Using BzMA and AA as examples, we illustrated that a monomer with a moderate k_p, whose polymer has a T_g close to room temperature leads to smooth dome-shaped particles whereas a monomer with a high k_p, whose polymer has a high T_g leads to a polymer shell encompassing an unreacted drop. A moderate k_p likely leads to shorter polymer chains that are well-solvated by the unreacted monomer, which, combined with the low T_g enables swift diffusion of monomer and thus isotropic evaporation during chamber evacuation, creating the smooth dome morphology. A high k_p means rapid conversion of monomer to polymer at the outer surface of a monomer drop, which, combined with the high T_g creates a solid shell that impedes further polymerization. Upon chamber evacuation, the shell collapses or breaks to let the unreacted (and thus volatile) monomer escape.

To further validate this correlation between the monomer reactivity/polymer property and the resulting particle morphology, we expanded our investigation to 7 other monomers and summarized their properties in Figure 5A. The corresponding particle morphologies captured

using SEM are shown in Figure 5B. The property combinations that lead to smooth dome formation, as highlighted in blue in Figure 5A, clearly point to the need for a moderate k_p and a moderate T_g simultaneously. Among the 9 monomers investigated, BzMA, 2-(dimethylamino)ethyl methacrylate (DMAEMA), 2-hydroxyethyl methacrylate (HEMA), glycidyl methacrylate (GMA), and cyclohexyl methacrylate (CHMA) all led to CDP particles with a smooth dome morphology, outlining the range of k_p values between 10^3 and $3*10^3$ L mol^{-1} s^{-1},[44,52] and the range of T_g values between 20 and 95 °C as the design space for such a particle morphology. If k_p exceeds this range with a relatively high T_g value, as demonstrated by AA, CDP would give rise to collapsed shells or a particle with granular morphology. If k_p exceeds this range with a low T_g, as demonstrated by butyl acrylate (BA) ($14.2*10^3$ L mol^{-1} s^{-1}, -54°C),[44] the as-formed polymer particles maintain their liquid-like behavior, as shown in Figure 5B for PBA. If k_p falls below this range, as demonstrated by Styrene (St) ($0.16*10^3$ L mol^{-1} s^{-1}, 100°C),[44] miniscule, underdeveloped polymer lumps emerge, pointing to insufficient conversion to polymer during CDP. Finally, if T_g exceeds this range, as demonstrated by (MAA) ($1.2*10^3$ L mol^{-1} s^{-1}, 228°C)[44], a granular morphology was obtained following CDP.[53] The polymer particles lose their circular shape and instead resemble aggregated clusters.

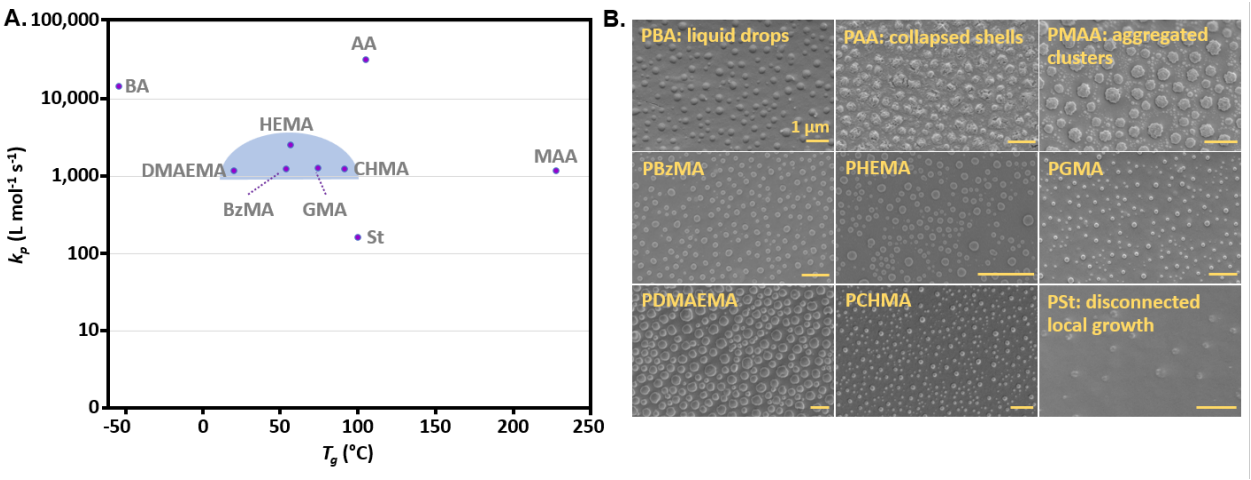

Figure 5. CDP particle morphologies as a function of the monomer propagation constant (k_p) and the reported polymer glass transition temperature (T_g), along with their corresponding SEM images. The zone of k_p and T_g combinations that give rise to a smooth dome-like particle morphology is highlighted in blue in A.

Finally, we characterized the molecular weight, using Gel Permeation Chromatography (GPC), of the polymer particles synthesized using two of the monomers mentioned above, i.e., GMA and BA (Table 1). These molecular weight data match the literature values for polymers synthesized via free radical polymerization mechanism using vacuum-based techniques (e.g., using iCVD or emulsion polymerization).[54–57] Therefore, we believe that the molecular weight obtained using CDP is consistent with the existing framework on free radical polymerization. This conclusion is further corroborated by the monomer-to-polymer conversion rate (Figure 3B), which demonstrates a linear dependence on the reaction time, indicating an absence of autoacceleration or the Trommsdorff-Norrish effect. As such, we believe CDP is chemically analogous to conventional free radical polymerization under the conditions reported in this work.

Table 1. Molecular weight and polydispersity of particles obtained via CDP.

Polymer	M_n (kDa)	M_w (kDa)	Polydispersity
PGMA	9.9	20.6	2.1
PBA	70.9	97.1	1.4

4. Conclusions

This work demonstrates process-structure-property relations in CDP that influence particle morphology by examining the surprising effects of vacuum-enabled removal of unreacted monomers with differing physicochemical properties. Partial conversion of monomer to polymer within the droplet followed by rapid evaporation of the unreacted monomer yielded either polymer domes or shells, as exemplified by CDP of BzMA and AA monomers. The disparate morphologies were established upon the evaporation of unreacted monomer, which we argue are influenced by the ease of diffusion of monomer within the polymer-rich droplet interface. This work also shows that dome-shaped polymer particles can be synthesized in CDP with diameters in the micrometer range and could serve as a platform for studies of anisotropic self-assembled particle structures.

Unprecedented particle morphology control was demonstrated using CDP, which fills a gap in morphology control for non-spherical polymer particles in the existing literature. Fundamentally, this work revealed that polymerization in a monomer micro-drop could undergo two distinct pathways. For systems with low to moderate k_p and T_g, the polymerization is relatively isotropic, whereas high k_p and T_g lead to severe spatial heterogeneity of polymerization. This insight could inform the understanding of other polymerization techniques, such as mini-emulsion polymerization. Technologically, this work demonstrated the power of in-situ characterization during synthesis for revealing key mechanistic insights. This work represents one of the first cases

of implementing in-situ and real-time microscopy in CVD polymerization, pointing to an exciting prospect with the broad adoption of in-situ imaging during polymer synthesis.

Numerous variables that dictate polymer particle morphology can be controlled uniquely within a CDP reactor and provide opportunities for further study. The spatial separation of the radical production from the monomer droplets decouples the thermal energy required for initiator decomposition from the temperature at which the droplet is controlled. Such a setup will enable the investigation of bulk monomer polymerization kinetics in droplets across a wide range of temperatures. The properties of the resulting polymer (e.g., molecular weight, branching, end groups, stiffness) are a consequence of the relative rates of initiation, propagation, termination, and chain transfer. Our previous study showed an abundance of chain transfer or disproportionation events compared to combination,[27] and we have reserved in-depth analysis of the kinetic parameters associated with individual reactions for future work. Future studies should also probe a broad spectrum of properties in the particles (e.g., molecular weight, porosity) to understand how upstream CDP parameters can be used to control them.

Polymer particles made by the CDP technique can be synthesized from monomer precursors in less than one minute, the rapidity of which provides a distinct advantage over convention liquid-based syntheses.[58] With rapid polymerization of monomer droplets to polymer domes and shells across multiple orders of magnitude in diameter, CDP is poised to impact studies of polymer particles spanning fundamental to applied research, spanning the self-assembly of anisotropic and chemically functionalized particles with programmable shapes[59–61] to their application in healthcare,[62,63] agriculture,[64] and food science.

Acknowledgments

The authors acknowledge funding from the National Science Foundation Faculty Early Career Development Program (CMMI-2144171). This material is also based upon work supported by the National Science Foundation Graduate Research Fellowship program (DGE-1650441). Analytical methods involved the use of the Cornell Center for Materials Research (CCMR) Shared Facilities which are supported through the NSF MRSEC program (DMR-1719875).

Supporting Information Available: CDP steps and process conditions diagram, FTIR and Raman spectra identifying polymer particle composition, contact angle of monomers on perfluorinated substrate, CDP radical chain polymerization reactions. This material is available free of charge *via* the Internet at http://pubs.acs.org.

Corresponding Author:

Rong Yang – ryang@cornell.edu

Author Contributions:

T.F. conducted all other experiments and characterization. Both authors, T.F. and R.Y., contributed to the study design, data analysis, and manuscript drafting and editing.

References

(1) Sur, S.; Rathore, A.; Dave, V.; Reddy, K. R.; Chouhan, R. S.; Sadhu, V. Recent Developments in Functionalized Polymer Nanoparticles for Efficient Drug Delivery System. *Nano-Structures and Nano-Objects* **2019**, *20*, 100397.

(2) Deirram, N.; Zhang, C.; Kermaniyan, S. S.; Johnston, A. P. R.; Such, G. K. PH-Responsive Polymer Nanoparticles for Drug Delivery. *Macromol. Rapid Commun.* **2019**,

40 (10), 1800917.

(3) Calzoni, E.; Cesaretti, A.; Polchi, A.; Di Michele, A.; Tancini, B.; Emiliani, C. Biocompatible Polymer Nanoparticles for Drug Delivery Applications in Cancer and Neurodegenerative Disorder Therapies. *J. Funct. Biomater.* **2019**, *10* (1), 4.

(4) Ali, I.; Alsehli, M.; Scotti, L.; Scotti, M. T.; Tsai, S. T.; Yu, R. S.; Fa Hsieh, M.; Chen, J. C. Progress in Polymeric Nano-Medicines for Theranostic Cancer Treatment. *Polymers.* **2020**, *12* (3), 598.

(5) Gauger, A. J.; Hershberger, K. K.; Bronstein, L. M. Theranostics Based on Magnetic Nanoparticles and Polymers: Intelligent Design for Efficient Diagnostics and Therapy. *Front. Chem.* **2020**, *8*, 561.

(6) Paisley, N. R.; Tonge, C. M.; Hudson, Z. M. Stimuli-Responsive Thermally Activated Delayed Fluorescence in Polymer Nanoparticles and Thin Films: Applications in Chemical Sensing and Imaging. *Front. Chem.* **2020**, *8*, 229.

(7) Liu, X.; Zheng, W.; Kumar, R.; Kumar, M.; Zhang, J. Conducting Polymer-Based Nanostructures for Gas Sensors. *Coord. Chem. Rev.* **2022**, *462*, 214517.

(8) Fan, W.; Tong, X.; Farnia, F.; Yu, B.; Zhao, Y. CO2-Responsive Polymer Single-Chain Nanoparticles and Self-Assembly for Gas-Tunable Nanoreactors. *Chem. Mater.* **2017**, *29* (13), 5693–5701.

(9) Spirescu, V. A.; Chircov, C.; Grumezescu, A. M.; Andronescu, E. Polymeric Nanoparticles for Antimicrobial Therapies: An up-to-Date Overview. *Polymers.* **2021**, *13* (5), 724.

(10) Kapate, N.; Clegg, J. R.; Mitragotri, S. Non-Spherical Micro- and Nanoparticles for Drug Delivery: Progress over 15 Years. *Adv. Drug Deliv. Rev.* **2021**, *177*, 113807.

(11) Zhu, X.; Vo, C.; Taylor, M.; Smith, B. R. Non-Spherical Micro- and Nanoparticles in Nanomedicine. *Mater. Horizons* **2019**, *6* (6), 1094–1121.

(12) Daum, N.; Tscheka, C.; Neumeyer, A.; Schneider, M. Novel Approaches for Drug Delivery Systems in Nanomedicine: Effects of Particle Design and Shape. *Wiley Interdiscip. Rev. Nanomedicine Nanobiotechnology* **2012**, *4* (1), 52–65.

(13) Dendukuri, D.; Pregibon, D. C.; Collins, J.; Hatton, T. A.; Doyle, P. S. Continuous-Flow Lithography for High-Throughput Microparticle Synthesis. *Nat. Mater.* **2006**, *5* (5), 365–369.

(14) Lesov, I.; Valkova, Z.; Vassileva, E.; Georgiev, G. S.; Ruseva, K.; Simeonov, M.; Tcholakova, S.; Denkov, N. D.; Smoukov, S. K. Bottom-Up Synthesis of Polymeric Micro- and Nanoparticles with Regular Anisotropic Shapes. *Macromolecules* **2018**, *51* (19), 7456–7462.

(15) Yunker, P. J.; Still, T.; Lohr, M. A.; Yodh, A. G. Suppression of the Coffee-Ring Effect by Shape-Dependent Capillary Interactions. *Nature* **2011**, *476* (7360), 308–311.

(16) Safari, H.; Kelley, W. J.; Saito, E.; Kaczorowski, N.; Carethers, L.; Shea, L. D.; Eniola-

Adefeso, O. Neutrophils Preferentially Phagocytose Elongated Particles—An Opportunity for Selective Targeting in Acute Inflammatory Diseases. *Sci. Adv.* **2023**, *6* (24), eaba1474.

(17) Tang, Y.; Varyambath, A.; Ding, Y.; Chen, B.; Huang, X.; Zhang, Y.; Yu, D. G.; Kim, I.; Song, W. Porous Organic Polymers for Drug Delivery: Hierarchical Pore Structures, Variable Morphologies, and Biological Properties. *Biomater. Sci.* **2022**, *10* (19), 5369–5390.

(18) Hueckel, T.; Hocky, G. M.; Sacanna, S. Total Synthesis of Colloidal Matter. *Nat. Rev. Mater.* **2021**, *6* (11), 1053–1069.

(19) Patil, A.; Dyawanapelly, S.; Dandekar, P.; Jain, R. Fabrication and Characterization of Non-Spherical Polymeric Particles. *J. Pharm. Innov.* **2021**, *16* (4), 747–758.

(20) Champion, J. A.; Katare, Y. K.; Mitragotri, S. Making Polymeric Micro- and Nanoparticles of Complex Shapes. *Proc. Natl. Acad. Sci.* **2007**, *104* (29), 11901–11904.

(21) Yamashita, N.; Konishi, N.; Tanaka, T.; Okubo, M. Preparation of Hemispherical Polymer Particles by Cleavage of a Janus Poly(Methyl Methacrylate) /Polystyrene Composite Particle. *Langmuir* **2012**, *28* (35), 12886–12892.

(22) Chen, W.-H.; Tu, F.; Bradley, L. C.; Lee, D. Shape-Tunable Synthesis of Sub-Micrometer Lens-Shaped Particles via Seeded Emulsion Polymerization. *Chem. Mater.* **2017**, *29* (7), 2685–2688.

(23) Hou, P. X.; Zhang, F.; Zhang, L.; Liu, C.; Cheng, H. M. Synthesis of Carbon Nanotubes by Floating Catalyst Chemical Vapor Deposition and Their Applications. *Adv. Funct. Mater.* **2022**, *32* (11), 2108541.

(24) Jamkhande, P. G.; Ghule, N. W.; Bamer, A. H.; Kalaskar, M. G. Metal Nanoparticles Synthesis: An Overview on Methods of Preparation, Advantages and Disadvantages, and Applications. *J. Drug Deliv. Sci. Technol.* **2019**, *53*, 101174.

(25) Haller, P. D.; Gupta, M. Synthesis of Polymer Nanoparticles via Vapor Phase Deposition onto Liquid Substrates. *Macromol. Rapid Commun.* **2014**, *35* (23), 2000–2004.

(26) Tung, H.-Y.; Guan, Z.-Y.; Liu, T.-Y.; Chen, H.-Y. Vapor Sublimation and Deposition to Build Porous Particles and Composites. *Nat. Commun.* **2018**, *9* (1), 2564.

(27) Franklin, T.; Streever, D. L.; Yang, R. Versatile and Rapid Synthesis of Polymer Nanodomes via Template- and Solvent-Free Condensed Droplet Polymerization. *Chem. Mater.* **2022**, *34* (13), 5960–5970.

(28) Lovell, P. A.; Schork, F. J. Fundamentals of Emulsion Polymerization. *Biomacromolecules* **2020**, *21* (11), 4396–4441.

(29) Luk, B. T.; Zhang, L. Current Advances in Polymer-Based Nanotheranostics for Cancer Treatment and Diagnosis. *ACS Appl. Mater. Interfaces* **2014**, *6* (24), 21859–21873.

(30) Guerra, F. D.; Attia, M. F.; Whitehead, D. C.; Alexis, F. Nanotechnology for Environmental Remediation: Materials and Applications. *Molecules* **2018**, *23* (7), 1760.

(31) Ulrich, S.; Stoll, S.; Pefferkorn, E. Computer Simulations of Homogeneous Deposition of

Liquid Droplets. *Langmuir* **2004**, *20* (5), 1763–1771.

(32) Castillo, J. E.; Weibel, J. A.; Garimella, S. V. The Effect of Relative Humidity on Dropwise Condensation Dynamics. *Int. J. Heat Mass Transf.* **2015**, *80*, 759–766.

(33) P Meakin. Dropwise Condensation: The Deposition Growth and Coalescence of Fluid Droplets. *Phys. Scr.* **1992**, *1992* (T44), 31.

(34) Betz, A. R. The Role of Droplet Dynamics in Condensation Frosting. In *Ice Adhesion*; 2020; pp 135–160.

(35) Bhat, G.; Kandagor, V. Synthetic Polymer Fibers and Their Processing Requirements. In *Advances in Filament Yarn Spinning of Textiles and Polymers*; Woodhead Publishing, 2014; pp 3–30.

(36) Odian, G. Radical Chain Polymerization. In *Principles of Polymerization*; Wiley Online Books; John Wiley & Sons, Inc., 2004; pp 198–349.

(37) Van Berkel, K. Y.; Russell, G. T.; Gilbert, R. G. Entry in Emulsion Polymerization: Effects of Initiator and Particle Surface Charge. *Macromolecules* **2003**, *36* (11), 3921–3931.

(38) Achilias, D. S.; Kiparissides, C. Development of a General Mathematical Framework for Modeling Diffusion-Controlled Free-Radical Polymerization Reactions. *Macromolecules* **1992**, *25* (14), 3739–3750.

(39) Kubečka, J.; Uhlík, F.; Košovan, P. Mean Squared Displacement from Fluorescence Correlation Spectroscopy. *Soft Matter* **2016**, *12* (16), 3760–3769.

(40) Morton, M.; Kaizerman, S.; Altier, M. W. Swelling of Latex Particles. *J. Colloid Sci.* **1954**, *9* (4), 300–312.

(41) Stricker, L.; Grillo, F.; Marquez, E. A.; Panzarasa, G.; Smith-Mannschott, K.; Vollmer, J. Universality of Breath Figures on Two-Dimensional Surfaces: An Experimental Study. *Phys. Rev. Res.* **2022**, *4* (1), L012019.

(42) Ballard, M. J.; Gilbert, R. G.; Napper, D. H.; Pomery, P. J.; O'Sullivan, P. W.; O'Donnell, J. H. Propagation Rate Coefficients from Electron Spin Resonance Studies of the Emulsion Polymerization of Methyl Methacrylate. *Macromolecules* **1986**, *19* (5), 1303–1308.

(43) Karlsson, O. J.; Stubbs, J. M.; Karlsson, L. E.; Sundberg, D. C. Estimating Diffusion Coefficients for Small Molecules in Polymers and Polymer Solutions. *Polymer (Guildf).* **2001**, *42* (11), 4915–4923.

(44) Beuermann, S.; Buback, M. Rate Coefficients of Free-Radical Polymerization Deduced from Pulsed Laser Experiments. *Prog. Polym. Sci.* **2002**, *27* (2), 191–254.

(45) Dušička, E.; Nikitin, A. N.; Lacík, I. Propagation Rate Coefficient for Acrylic Acid Polymerization in Bulk and in Propionic Acid by the PLP–SEC Method: Experiment and 3D Simulation. *Polym. Chem.* **2019**, *10* (43), 5870–5878.

(46) Zammit, M. D.; Davis, T. P.; Haddleton, D. M. Determination of the Propagation Rate

Coefficient (Kp) and Termination Mode in the Free-Radical Polymerization of Methyl Methacrylate, Employing Matrix-Assisted Laser Desorption Ionization Time-of-Flight Mass Spectrometry for Molecular Weight Distribution. *Macromolecules* **1996**, *29* (1), 492–494.

(47) Fox, T. G.; Flory, P. J. Second-Order Transition Temperatures and Related Properties of Polystyrene. I. Influence of Molecular Weight. *J. Appl. Phys.* **1950**, *21* (6), 581.

(48) Eisenberg, A.; Yokoyama, T.; Sambalido, E. Dehydration Kinetics and Glass Transition of Poly(Acrylic Acid). *J. Polym. Sci. Part A-1 Polym. Chem.* **1969**, *7* (7), 1717–1728.

(49) Maurer, J. J.; Eustace, D. J.; Ratcliffe, C. T. Thermal Characterization of Poly(Acrylic Acid). *Macromolecules* **1987**, *20* (1), 196–202.

(50) Kaya, I.; Pala, Ç. Y. Thermodynamics of Poly(Benzyl Methacrylate)-Probe Interactions at Different Temperatures by Using Inverse Gas Chromatography. *Fluid Phase Equilib.* **2014**, *374*, 63–69.

(51) Bergfelt, A.; Rubatat, L.; Brandell, D.; Bowden, T. Poly(Benzyl Methacrylate)-Poly[(Oligo Ethylene Glycol) Methyl Ether Methacrylate] Triblock-Copolymers as Solid Electrolyte for Lithium Batteries. *Solid State Ionics* **2018**, *321*, 55–61.

(52) Kockler, K. B.; Fleischhaker, F.; Barner-Kowollik, C. Free Radical Propagation Rate Coefficients of N-Containing Methacrylates: Are We Family? *Macromolecules* **2016**, *49* (22), 8572–8580.

(53) Fox, T. G.; Garrett, B. S.; Goode, W. E.; Gratch, S.; Kincaid, J. F.; Spell, A.; Stroupe, J. D. Crystalline Polymers of Methyl Methacrylate. *J. Am. Chem. Soc.* **1958**, *80* (7), 1768–1769.

(54) Gupta, M.; Gleason, K. K. Large-Scale Initiated Chemical Vapor Deposition of Poly(Glycidyl Methacrylate) Thin Films. *Thin Solid Films* **2006**, *515* (4), 1579–1584.

(55) Plessis, C.; Arzamendi, G.; Leiza, J. R.; Schoonbrood, H. A. S.; Charmot, D.; Asua, J. M. Seeded Semibatch Emulsion Polymerization of N-Butyl Acrylate. Kinetics and Structural Properties. *Macromolecules* **2000**, *33* (14), 5041–5047.

(56) Lau, K. K. S.; Gleason, K. K. Initiated Chemical Vapor Deposition (ICVD) of Poly(Alkyl Acrylates): A Kinetic Model. *Macromolecules* **2006**, *39* (10), 3695–3703.

(57) Former, C.; Castro, J.; Fellows, C. M.; Tanner, R. I.; Gilbert, R. G. Effect of Branching and Molecular Weight on the Viscoelastic Properties of Poly(Butyl Acrylate). *J. Polym. Sci. Part A Polym. Chem.* **2002**, *40* (20), 3335–3349.

(58) Wurm, F. R.; Weiss, C. K. Nanoparticles from Renewable Polymers. *Front. Chem.* **2014**, *2*, 49.

(59) Avendaño, C.; Liddell Watson, C. M.; Escobedo, F. A. Directed Self-Assembly of Spherical Caps via Confinement. *Soft Matter* **2013**, *9* (38), 9153–9166.

(60) McBride, J. M.; Avendaño, C. Phase Behaviour and Gravity-Directed Self Assembly of Hard Convex Spherical Caps. *Soft Matter* **2017**, *13* (10), 2085–2098.

(61) Hosein, I. D.; Liddell, C. M. Convectively Assembled Nonspherical Mushroom Cap-Based Colloidal Crystals. *Langmuir* **2007**, *23* (17), 8810–8814.

(62) Nunes, D.; Andrade, S.; Ramalho, M. J.; Loureiro, J. A.; Pereira, M. C. Polymeric Nanoparticles-Loaded Hydrogels for Biomedical Applications: A Systematic Review on In Vivo Findings. *Polymers (Basel).* **2022**, *14* (5), 1010.

(63) Fabozzi, A.; Della Sala, F.; Di Gennaro, M.; Solimando, N.; Pagliuca, M.; Borzacchiello, A. Polymer Based Nanoparticles for Biomedical Applications by Microfluidic Techniques: From Design to Biological Evaluation. *Polym. Chem.* **2021**, *12* (46), 6667–6687.

(64) Shakiba, S.; Astete, C. E.; Paudel, S.; Sabliov, C. M.; Rodrigues, D. F.; Louie, S. M. Emerging Investigator Series: Polymeric Nanocarriers for Agricultural Applications: Synthesis, Characterization, and Environmental and Biological Interactions. *Environ. Sci. Nano* **2020**, *7* (1), 37–67.

For Table of Contents Only: